Chapter 3: Experimental Hardware

The Single Beam Transport Experiment (SBTE) consists of

- a vacuum enclosure with pumps,
- an ion source and high voltage power supply,
- an array of five independently powered quadrupoles, M1–M5, to enable the beam to be matched from the source into the transport lattice,
- eighty-two quadrupoles, Q1 through Q82, in a periodic focusing lattice with their power supplies
- several types of diagnostic hardware, and
- an automated data acquisition system.

A sketch of the overall system layout is included in Fig. 3.1.

3.1 Vacuum System

The vacuum tanks were made of aluminum, seven in number, exclusive of the source chamber. The tanks housing the transport channel were 31 inches in height and 27 inches in width, measured internally. The one adjoining the source was made 5.5 feet in length, with the other six being six feet in length. The large transverse dimensions allowed for the possible inclusion of a cryopumping panel. Access ports were provided every 6 inches to permit almost any conceivable diagnostic configuration (see Fig. 3.2). Five Balzers turbopumps, model TP-510, each with a net pumping speed (after mounting on adapter flanges) of about 350 l/sec, were distributed along the beamline. Each tank was vacuum baked to about 120° C, attaining an ultimate pressure with one pump of 2–3 $\times$ 10^{-8} Torr, as indicated by ion gauge. The bakeout

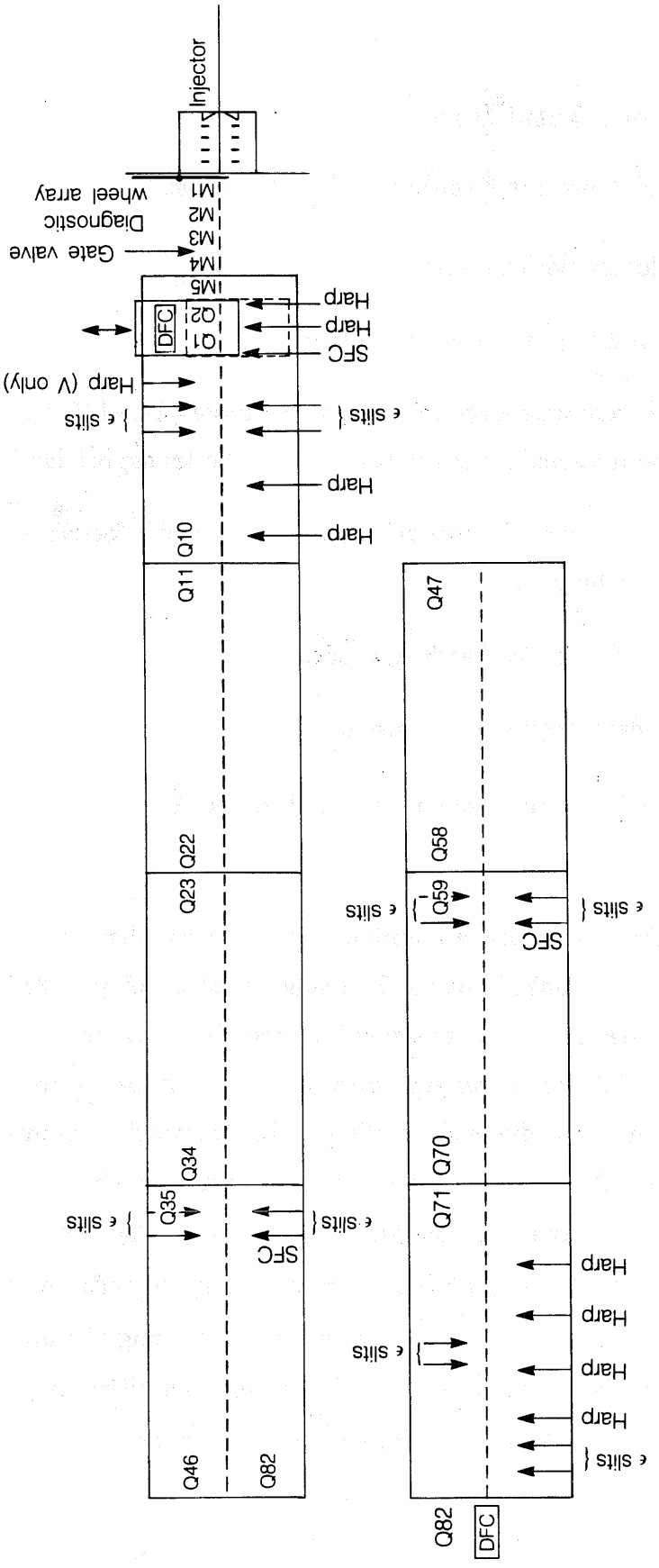

Figure 3.1: Physical layout of the SBTE lattice and diagnostics, showing the various charge collectors and beam profile diagnostics along the channel.

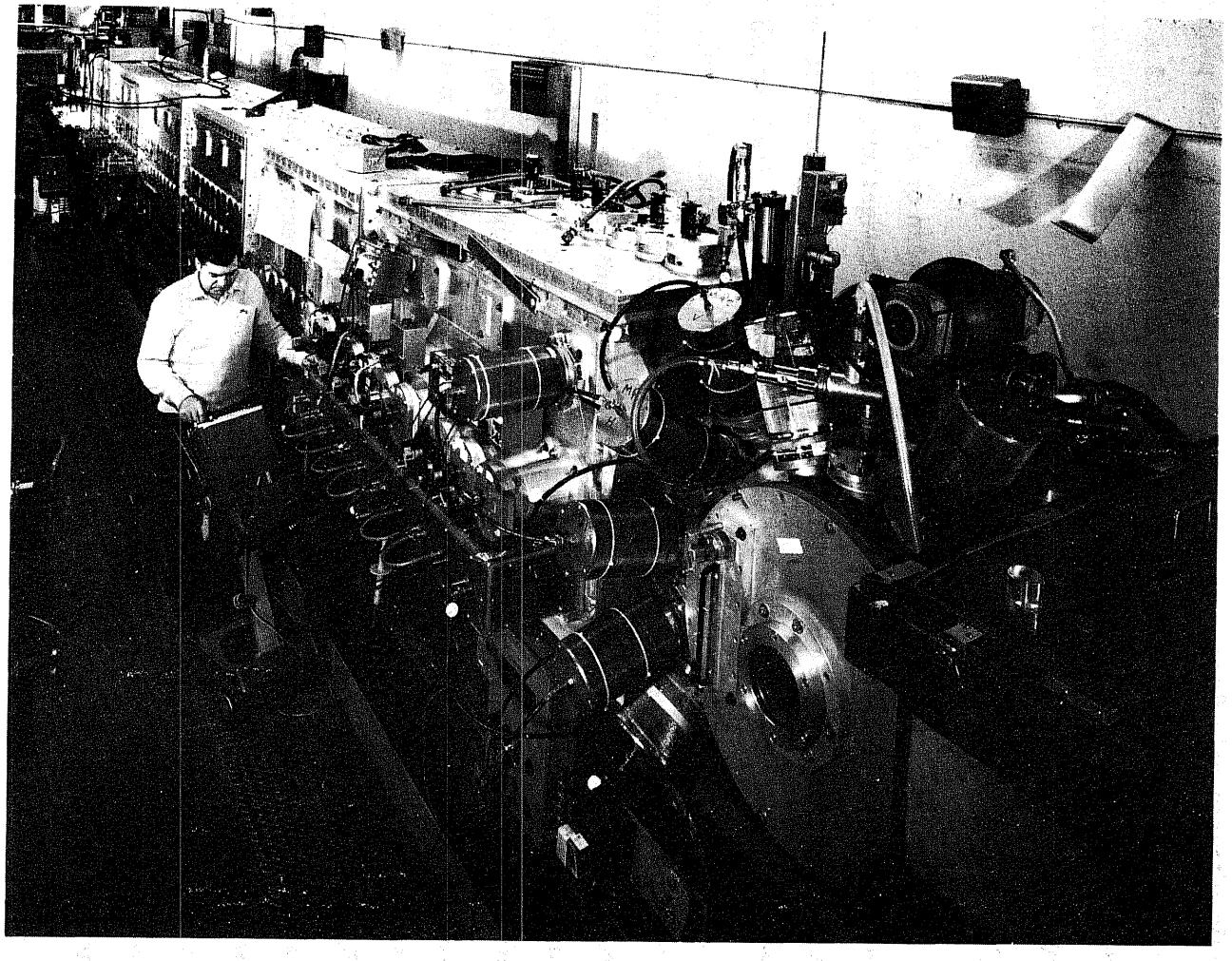

Figure 3.2: External view of the SBTE apparatus showing the vacuum chambers and diagnostic ports. Pumps are on the opposite side.

CBB 830-10596

procedure was not repeated after the tanks were installed on the beamline, for fear of distorting the quadrupole array (also aluminum). After adding two liquid nitrogen cold fingers to enhance water vapor pumping, the ultimate pressure was measured to be 8–10 $\times$ 10^{-8} Torr, with pressures of 2 $\times$ 10^{-7} Torr being more common. Background gas effects on the beam are discussed in sections 6.3 and 7.9.

3.2 Ion Source and Injector Assembly

A cesium-loaded alumino-silicate ion source was chosen on the basis of literature reports, confirmed by our own preliminary investigations, that many milliamperes per square centimeter of Cs^+ can be extracted in short pulse, low duty factor operation [32,33]. The intrinsically low gas load, simplicity of operation, potential availability of certain other ion species with minimal effort, and the commercial availability of usable sources were the deciding factors. Such solid-state sources have two decided advantages over gaseous sources, in that the gas load for the solid-state source is nearly negligible, and there is a well-defined emitter surface, having effectively zero equilibration time before coming into steady-state operation. Very short pulses are possible ($<$ 10 μsec), precluding any space-charge buildup due to ionizing collisions between beam and background gas particles. Although the SBTE quadrupoles are electrostatic, and hence provide large sweeping fields to clear static charges from the bore region, this short-pulse feature could be desirable in magnetically focused intense beam dynamics research. More information about these sources, the problems we encountered, and our solutions is provided in Appendix E.

A schematic diagram of the injector assembly (designed by C. Kim using Herrmannsfeldt's EGUN program [34]) is shown in Fig. 3.3, and an exploded view of the injector in Fig. 3.4. At the gun exit, up to three grids were

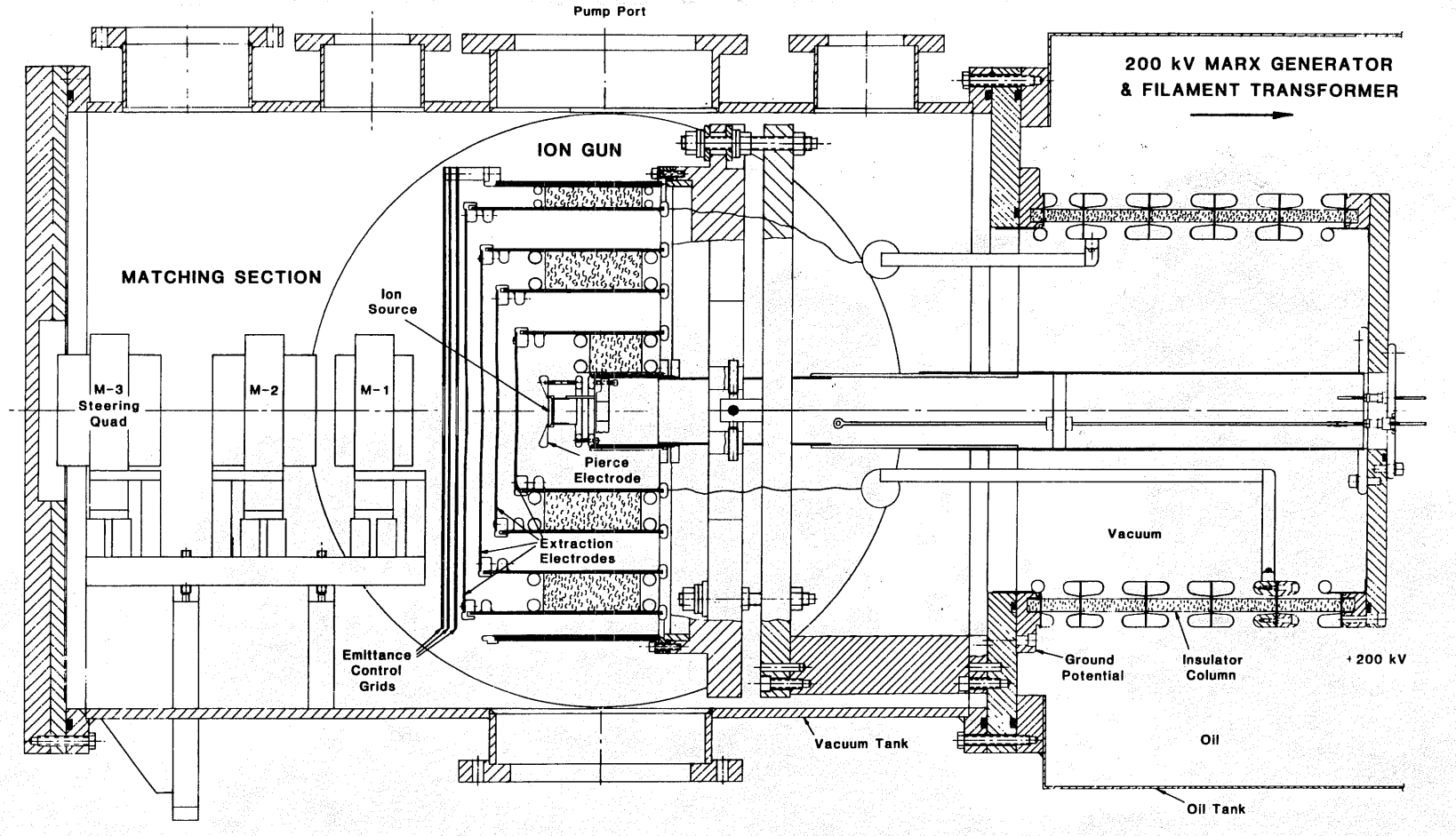

Figure 3.3: Schematic drawing of the SBTE injector, showing the concentric electrodes supporting the source and the focusing apertures.

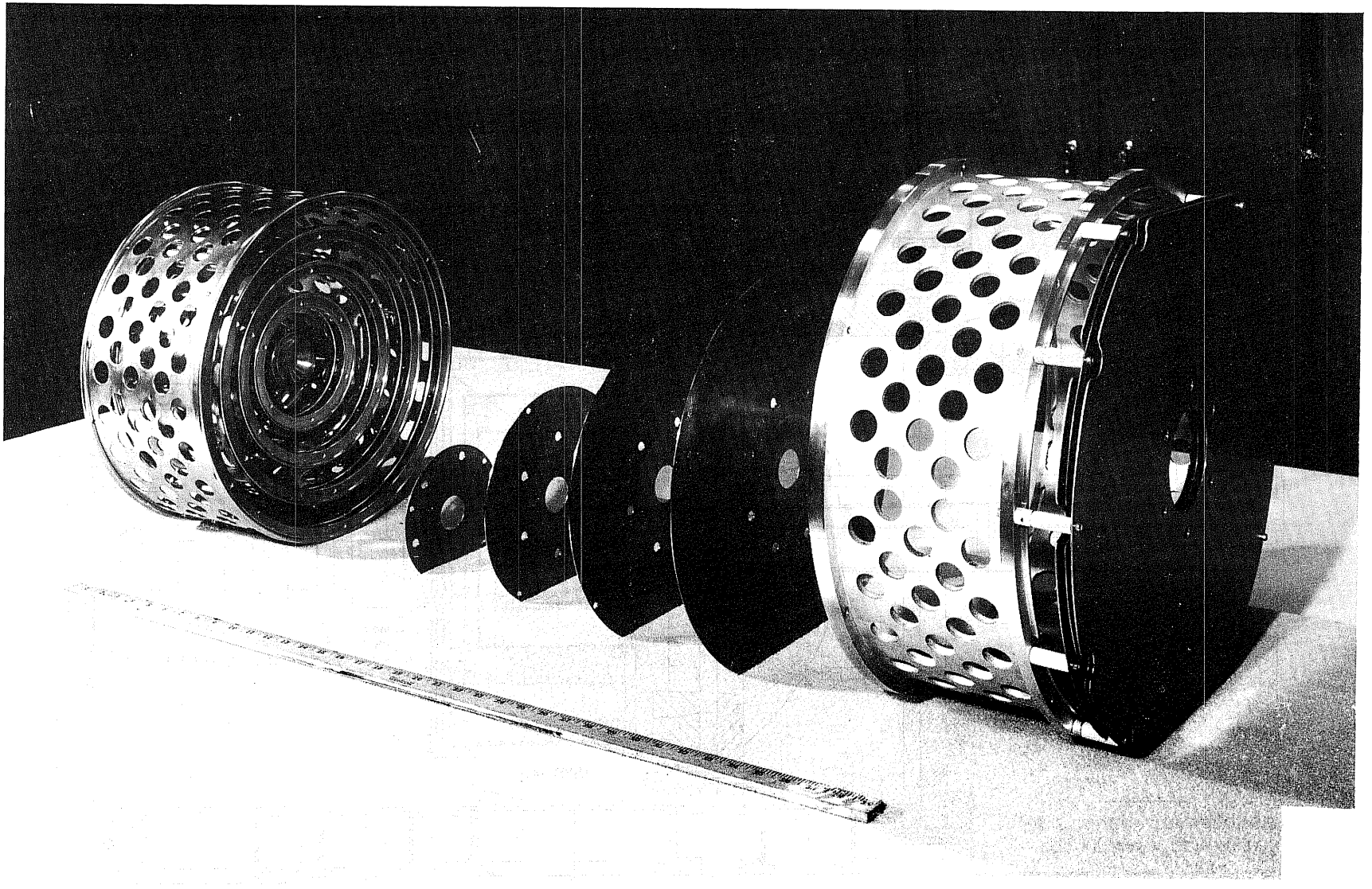

Figure 3.4: Exploded view of the SBTE injector, with the source visible at the center.

CBB 817-6741

provided, independently biasable for increasing the beam emittance prior to matching into the periodic channel. Grid perturbations to the emittance are discussed in Appendix C. They were used to change the beam emittance-to-current ratio continuously for the stability measurements reported in Ch. 5.

3.3 Marx generator

The high-voltage pulses (120–160 kV) used to generate the ion beam were provided by a Marx generator, schematically represented in Fig. 3.5. It consists of twelve capacitors connected in parallel by a network of charge-limiting resistors, with fast series connections made possible by triggering the breakdown of an array of spark gaps.

The high voltage pulse from the generator has a risetime of about 400 ns, providing a good approximation to the ideal applied voltage pulse required to minimize current and beam energy transients during the initiation of the diode [35]. The output voltage droops in time as the charge on the capacitors flows out along the charging resistors and through the spark gaps and load resistance. We used a capacitive divider to obtain the intermediate voltages we needed to grade the ion gun apertures. Any droop in beam energy results in debunching of the entire beam pulse, making corrections necessary to the measured current to detect beam loss along the lattice as explained in section 4.2.

3.4 Quadrupoles & Power Supplies

We chose to use electrostatic quadrupoles, as mentioned above, primarily for cost reasons, but there are advantages in terms of the focusing force available from an electrostatic system. The beam current in the space-charge dominated regime scales as $(R/L)^2$ for constant σ_0, and the required focusing gradient scales as $1/L$ for constant σ_0, where R is the bore radius and $2L$

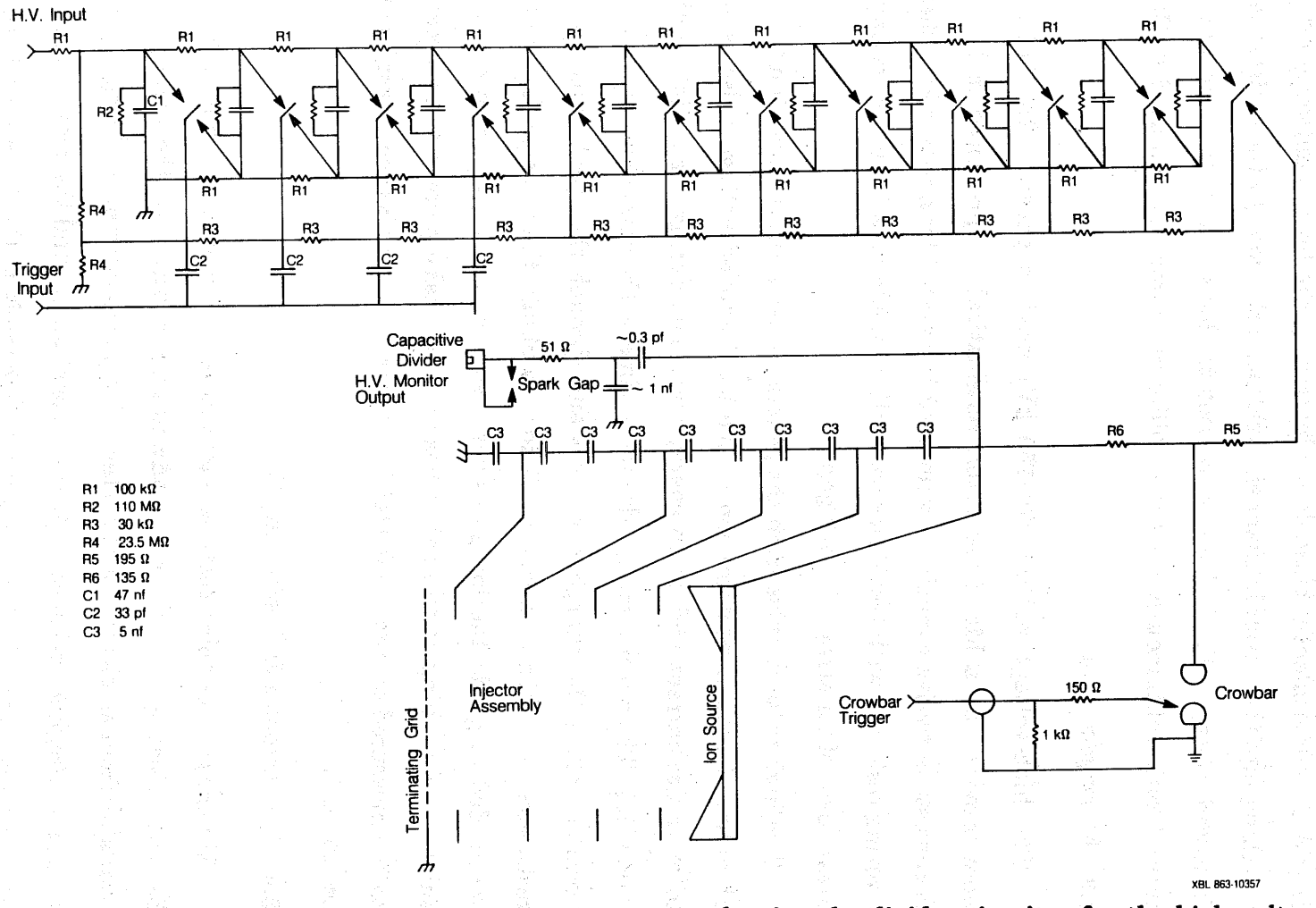

Figure 3.5: Circuit diagram for the SBTE Marx generator, showing the divider circuitry for the high voltage monitor and for the injector aperture voltages, as well as the triggers for the Marx itself and for the crowbar used to terminate the beam pulse.

is the lens period. We needed a short lattice period in order to fit as many periods as possible into the available experimental area and to keep the beam current high, making beam diagnosis easier. These requirements made large focusing forces desirable. At the low particle velocity we planned to use ($v \simeq 0.0014c$), the magnetic equivalent for the final geometry we chose would have required either pole-tip fields up to about 4 T or a much lower particle energy and beam current. The equivalent electric field of about 20 kV/cm was easily attainable.

The aim of the experiment was to measure the threshold for collective emittance degration in the most ideal linear field case possible. Short period and large bore requirements conflict with the desire to optimize focusing linearity. The bore and period of the lattice were chosen as a compromise between the desire to have a large enough beam size and current for ease of diagnosis, and the need to keep the period short as mentioned above. Maschke also made an experiment on beam transport, using a very small lattice bore [36], but by doing so he essentially eliminated the possibility of making detailed phase space measurements on the beam.

Dr. L. J. Laslett calculated a pole-tip shape to optimize the focusing linearity of the lattice, providing a focusing field approximately sinusoidal in z. The resulting electrodes have a length of 4 inches, a quadrupole bore diameter of 2 inches, and an inter-lens gap of 2 inches. The overall period of the lattice is therefore 12 inches. More details are given in Appendix D, including a diagram of the shape of the electrodes.

In order to use the acceptance of the channel efficiently, it was desirable to "match" the beam into the transport channel, that is, to launch the beam so that its envelope has the same periodicity as the channel. We used the first five quadrupoles for this purpose. For this matching section (labeled M1–

M5), the bore and spacing of certain quadrupoles are different from those in the periodic lattice, in order to ease the matching of very high space-charge beams into the periodic lattice. We found that M3–M5 could have the same dimensions as the periodic lattice quadrupoles, but M1 must be shorter in length (3 inches), M2 must be larger in bore (2.5 inches in diameter), and the spacing between M1 and M2 must be as small as practical (1.25 inches). In order to counter the space-charge defocusing, some large quadrupole strength is needed from the outset. By making M1 short and close to M2, the expansion of the beam dimension defocused in M1 is minimized. Providing a wide bore for M2 further relaxes the constraint on the allowable strength of M1, allowing the M1–M2 doublet enough strength to focus a high-current beam from the injector, even with an initially divergent envelope. The beam size in M3 is also calculated to become large in extreme cases, but the M2 constraint is calculated to be more severe. We also provided a separation between M3 and M4 of 2.5 inches to allow room for a gate valve, rather than using the periodic lattice spacing of 2.0 inches. This valve allowed access to the source housing while leaving the transport section under vacuum, greatly reducing the outgassing time required to return to high vacuum after working within the source chamber.

Four quadrupoles would be enough in principle to match the beam radius and convergence in each transverse dimension from the source into the periodic lattice. However, the use of a fifth independent matching element allowed additional control over the aperture requirements during matching. This freedom was useful later, when the beam began showing noticeable aberrations in focusing at the exit of the matching section as we tried to match the beam into lattices with $\sigma_0 \sim 90°$. This effect was reduced by weakening the M1–M2 doublet (see section 5.1.1), and may have been directly due to the matching section fields.

The transport quadrupoles were bench-mounted on I-beams, each beam holding 12 quadrupoles (see Fig. 3.6). The centers of the lenses were held at their nominal positions to within ±0.003 inch, and the relative lens rotation about the beam axis was held to ±3 milliradian. Each group of 12 quadrupoles was aligned within the vacuum tanks to within 0.010 inch using an optical surveying transit with precision targets.

All quadrupole power supplies are unregulated 30-kV supplies. They are used in ± pairs to maintain a true ground potential along the beam axis, apart from the beam potential. The connection to the quadrupoles is made through a filter and monitor network shown in Fig. 3.7.

3.5 Diagnostics

Diagnostic equipment consisted of various beam collimators, charge collectors, and also a multiwire scanner ("harp") used in the secondary electron emission mode. Two types of free-standing Faraday cups were used—shallow Faraday cups (SFC's), with grids for secondary electron control, and deep Faraday cups (DFC's), which were gridless, but electrostatically insulated for electron control.

3.5.1 Multiwire Profile Monitor

The multiwire profile scanner ("harp") is an array of thirty wires 2 inches in length and 0.010 inches in diameter, with a spacing between centers of 0.050 inches. The wires are individually connected to a 1000-Ω termination across the input terminals of a follow-and-hold circuit, as shown in Fig. 3.8. The various signal levels are frozen in when the follow-and-hold array is triggered, and then multiplexed on a 50-Ω coaxial cable to a digitizing storage oscilloscope. A minicomputer then reads the signal levels from the digitizer for calculation of the beam centroid and RMS radius. For one small subset of the data, we also examined the third moment of the transverse distribution

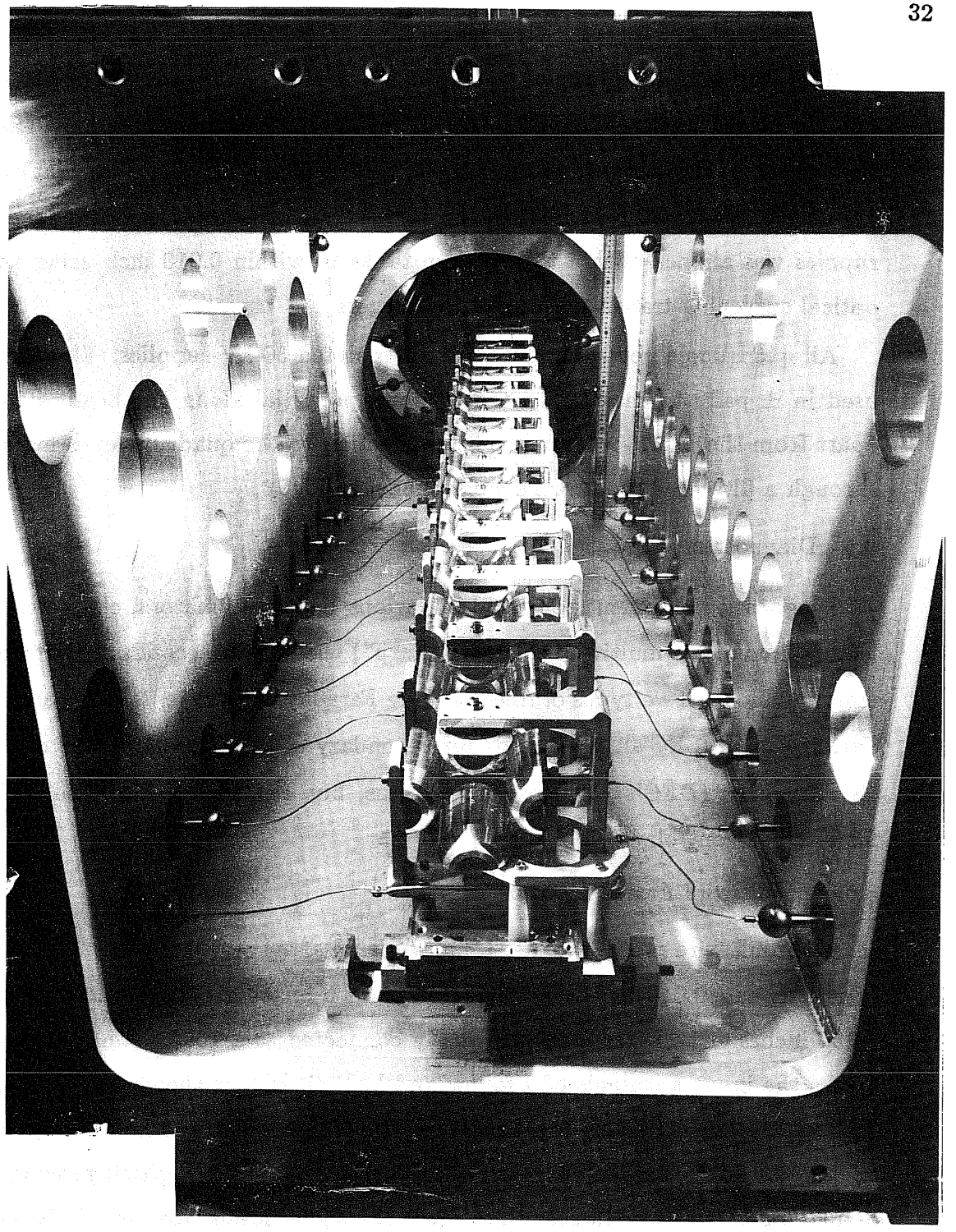

Figure 3.6: Interior of one of the SBTE vacuum tanks with quadrupole array installed. The length of each quadrupole electrode is 4 inches, and the bore radius is 1 inch.

CBB 831-845

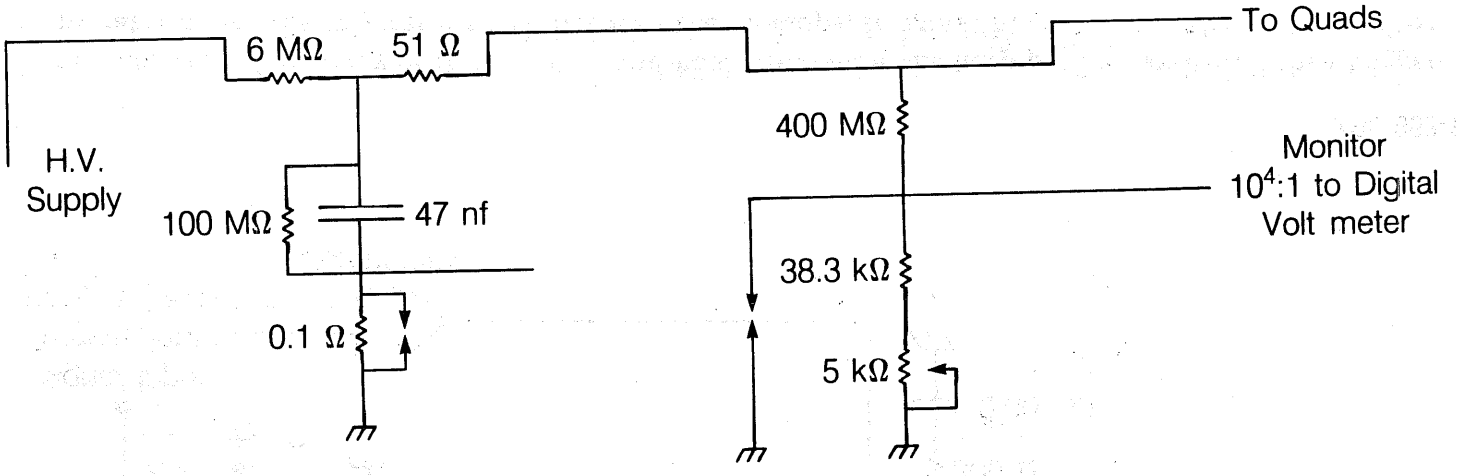

Figure 3.7: Circuit diagram for the SBTE quadrupole power supply and monitor chain. The 47-nf capacitor serves to hold the quadrupole potential constant in case of beam-induced currents. The monitor circuit measures the voltage applied to the quadrupoles.

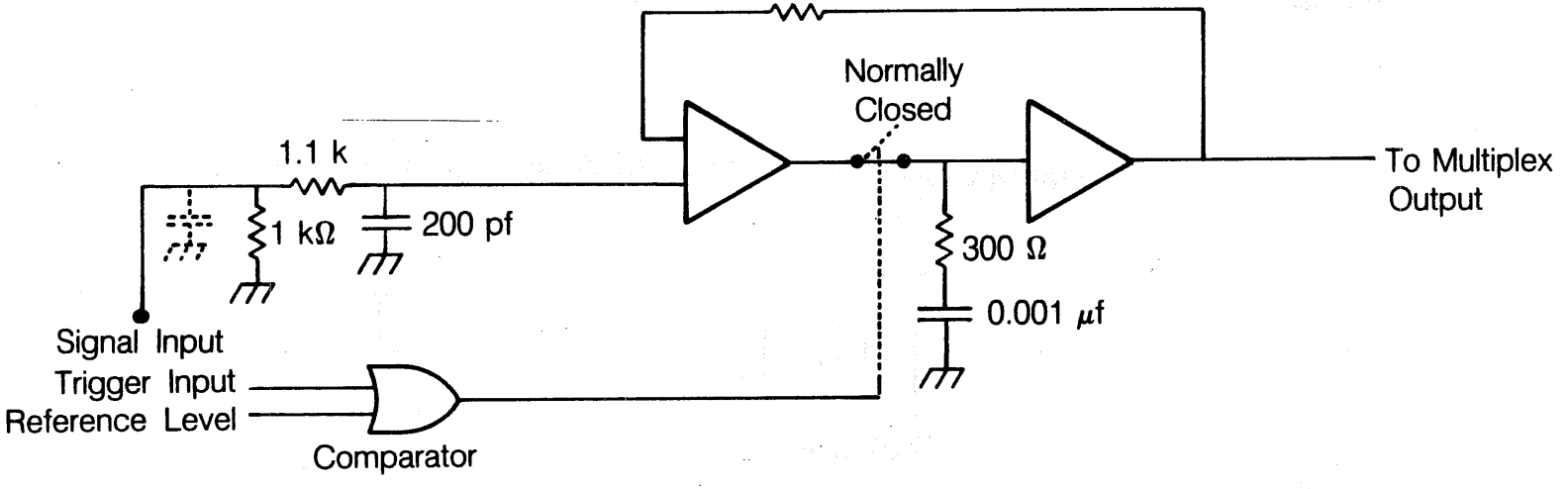

XBL 863-10354

Figure 3.8: One of an array of thirty follow-and-hold circuits for the harp profile monitor. When triggered, the comparator opens the transistor swich between the op-amps, freezing the voltage on the 1-nf capacitor.

for comparison with analytical results for a sextupole-symmetry beam mode with a non-zero third moment (see Figs. 5.5 and 5.4). We also used the emittance diagnostics to measure beam profiles.

3.5.2 Beam current monitors

The SFC's (Fig. 3.9) must be thin enough for insertion into the 2-inch gap between quadrupoles, which have electrodes at ±15-kV potentials, without shorting out the quadrupoles. Grids were required to shield the collector from the quadrupole fields and to provide a bias field to retain the secondary electrons on the main collector. These grids have an overall transparency of between 90% and 96%. The high yield of secondary electrons (measured to be about 11 per ion impact for 120–160 keV cesium ions normally incident on stainless steel) could have had a 50% effect on the measured beam current. The gridless DFC's (shown in Fig. 3.10) provided a current measurement with errors due primarily to secondary positive ion emission. These DFC's were designed by Kim, using the EGUN program [34], to provide secondary electron control by electrostatic effects, without inserting grids into the beam.

We placed gridded shallow Faraday cups, varying in grid transparency and mechanical design, along the lattice after Q2, Q6, Q36, and Q60. The two identical deep Faraday cups were placed after M5 and at the end of the lattice after Q82. We could install one of the DFCs within the lattice only by providing for a precision transverse-traveling mount holding the DFC itself and the two quadrupoles displaced by the DFC. We mounted Q1, Q2, and the DFC on a metal plate and aligned the plate carefully within the quadrupole lattice. Transverse motion was provided by a ball screw in the same manner as for the other diagnostics. These two cups provided direct confirmation of constancy of the beam current through the lattice observed at the lower σ_0 values. This constant beam current was used to intercal-

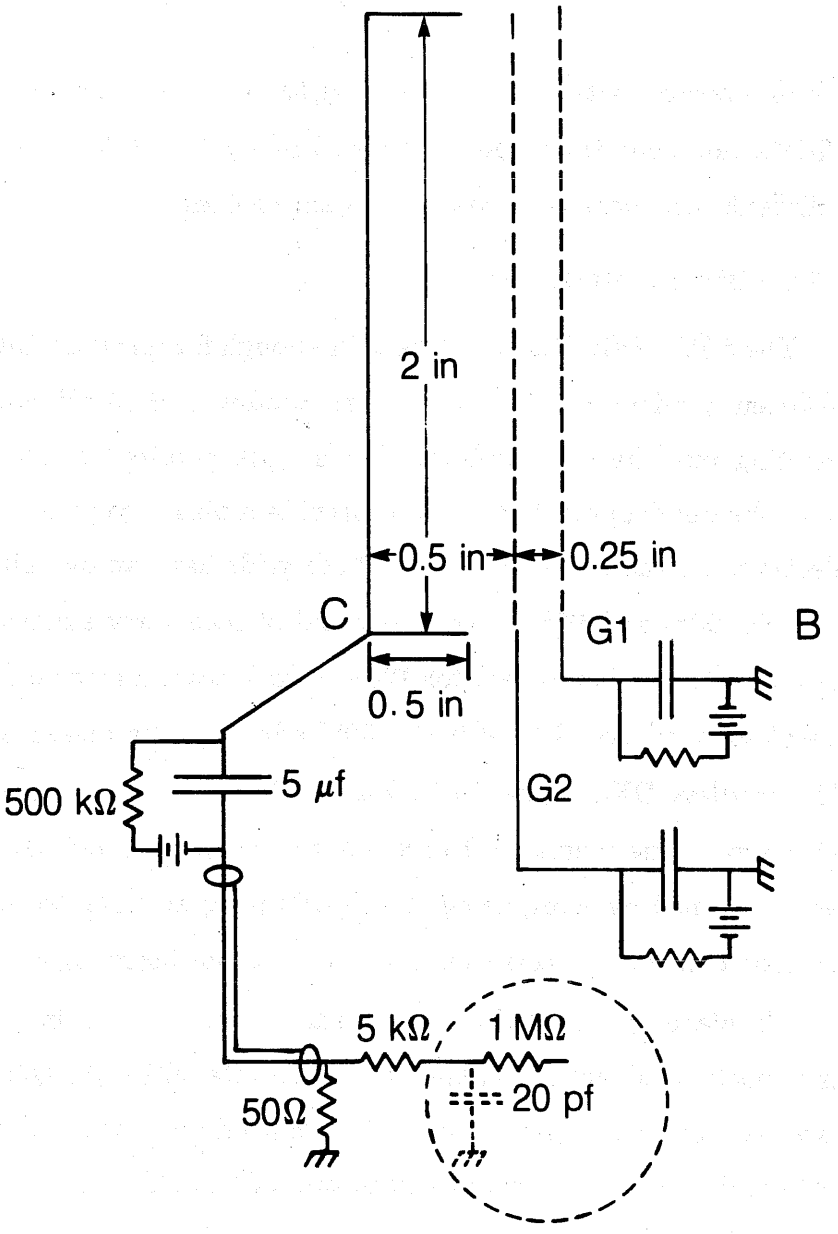

XBL 864-10367

Figure 3.9: Diagram of the shallow Faraday cup, including bias and signal-measurement circuitry. The 5-kΩ resistor in series with the oscilloscope (represented by the dotted circle) served as a 100-ns filter.

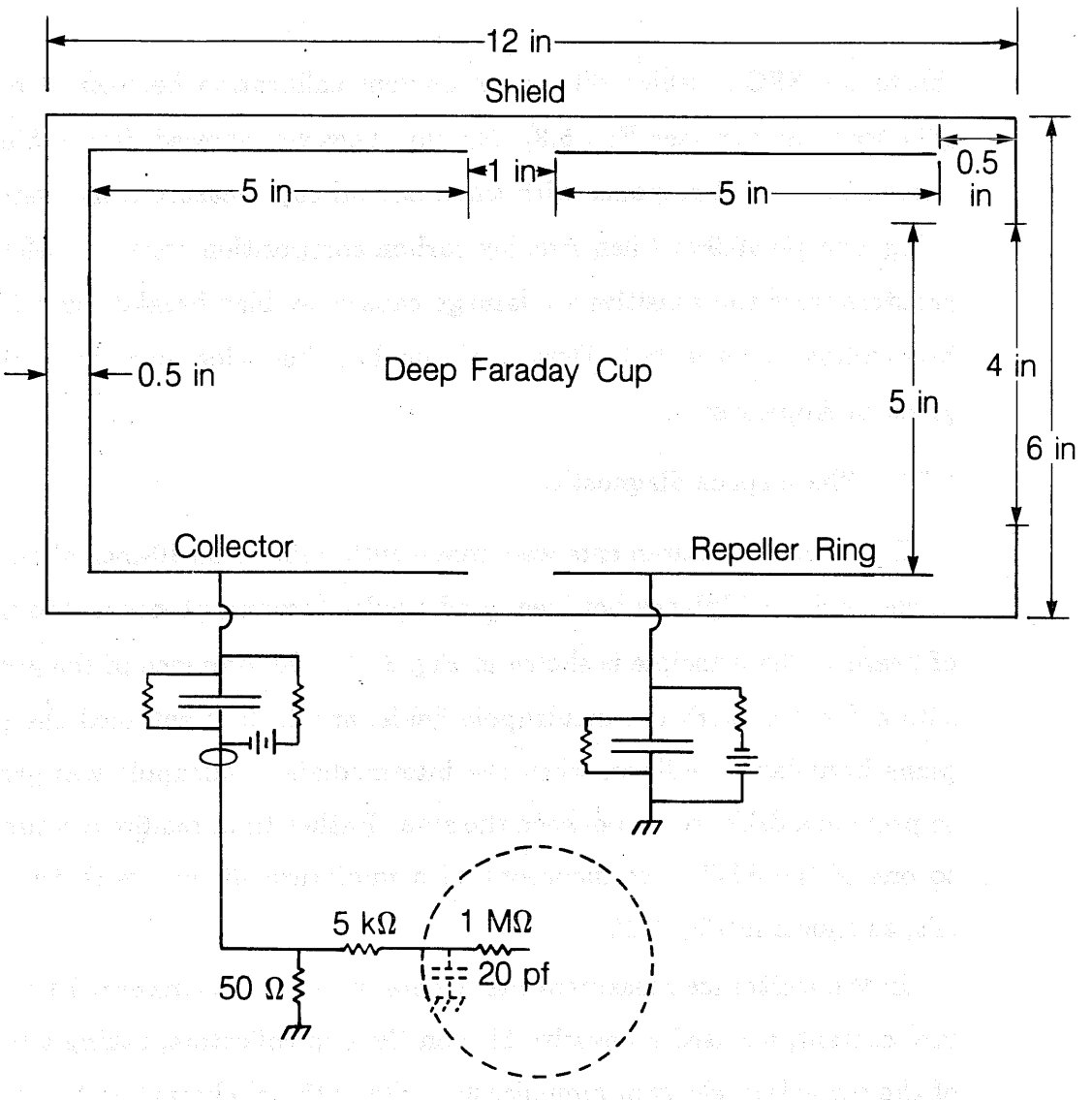

Deep Faraday Cup with Bias and Detector Circuitry

XBL 863-10355

Figure 3.10: Diagram of the deep Faraday cup. Gridless design required deep electrodes to provide bias for electron control. The typical operating potentials were ±2 kV on the collector and repeller, respectively.

ibrate the SFC's, which differed in current calibration becuase of differing grid transparency (see Fig. 5.3). No cup, however, showed detectable variation in its current response with time, and all cup measurements were made using a single 49.9-Ω Allen Bradley carbon composition resistor. (Metal-film resistors were too sensitive to damage caused by bias breakdown and other high-voltage transients.) Details of cup bias behavior and calibration are given in Appendix B.

3.5.3 Phase space diagnostics

Emittance measurements were made with pairs of 0.010-inch slits, placed in successive midplanes between quadrupoles (ground planes in the absence of beam). The principle is shown in Fig. 3.11. The presence of the grounded slits did not disturb the quadrupole fields, and in fact enforced the ground plane boundary condition when the intermediate quadrupole was grounded to provide a drift region between the slits. Rather than require a second drift to one of the SFC's, we incorporated a miniature slit cup with the second slit, as shown in Fig. 3.12.

In the emittance measurements, where we were not concerned with absolute current, we used a negative bias on the cup collectors, taking advantage of the secondary electron amplification. Operational characteristics and bias response are discussed further in Appendix B.

3.5.4 Diagnostic positioning

The diagnostics were positioned within the vacuum system along ball screws, with the driving torque applied from the outside using commercially available ferrifluidic seals, having a very low gas leakage. The positioning precision within the beamline was within ±0.002 inch.

Principle of Two-slit Emittance Measurement Technique

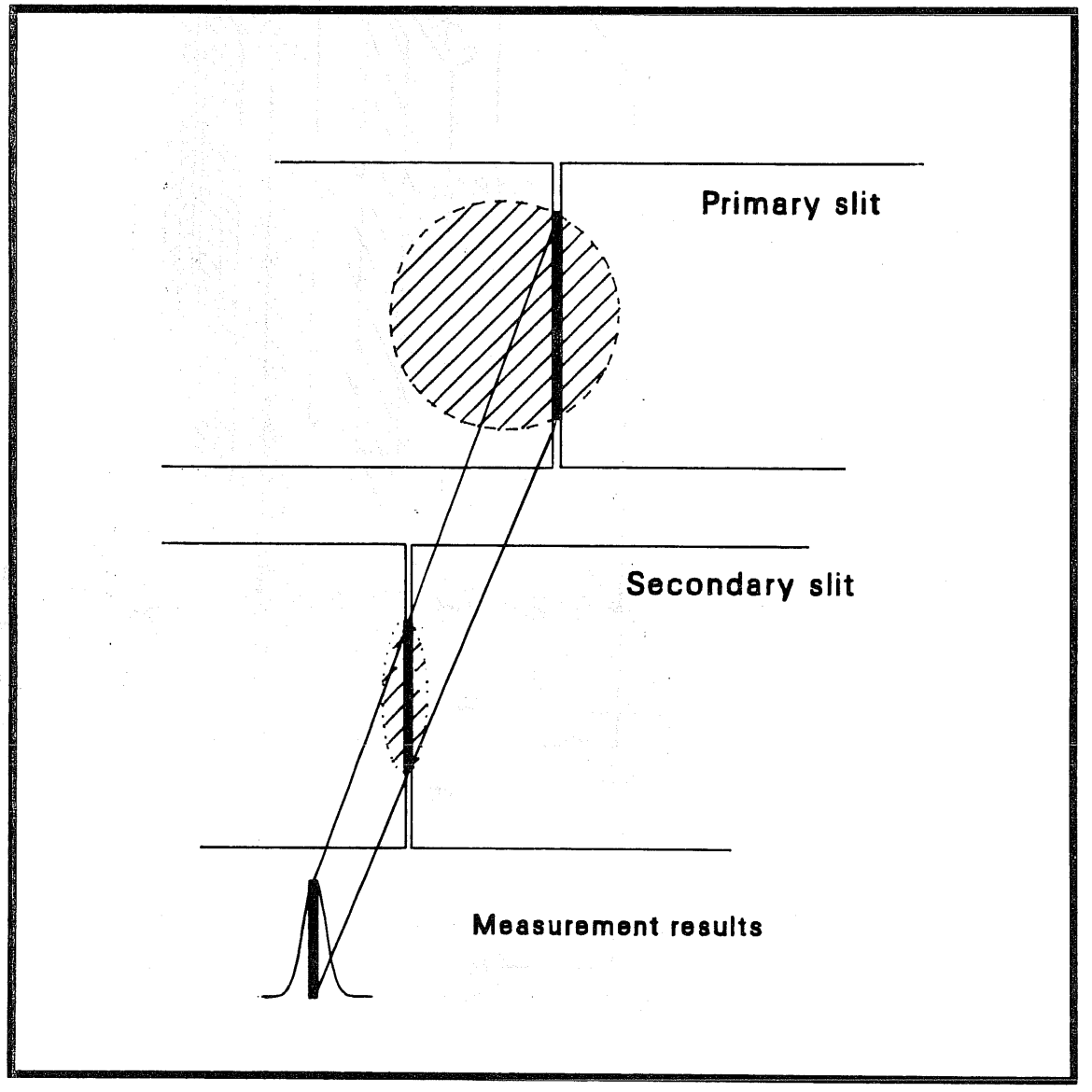

XBL 865-1843

Figure 3.11: Illustration of the principle of the two-slit phase space measurement technique. The particles are collimated in position by the upstream slit, and the downstream slit passes those particles into the detector which have a certain well-defined transverse velocity.

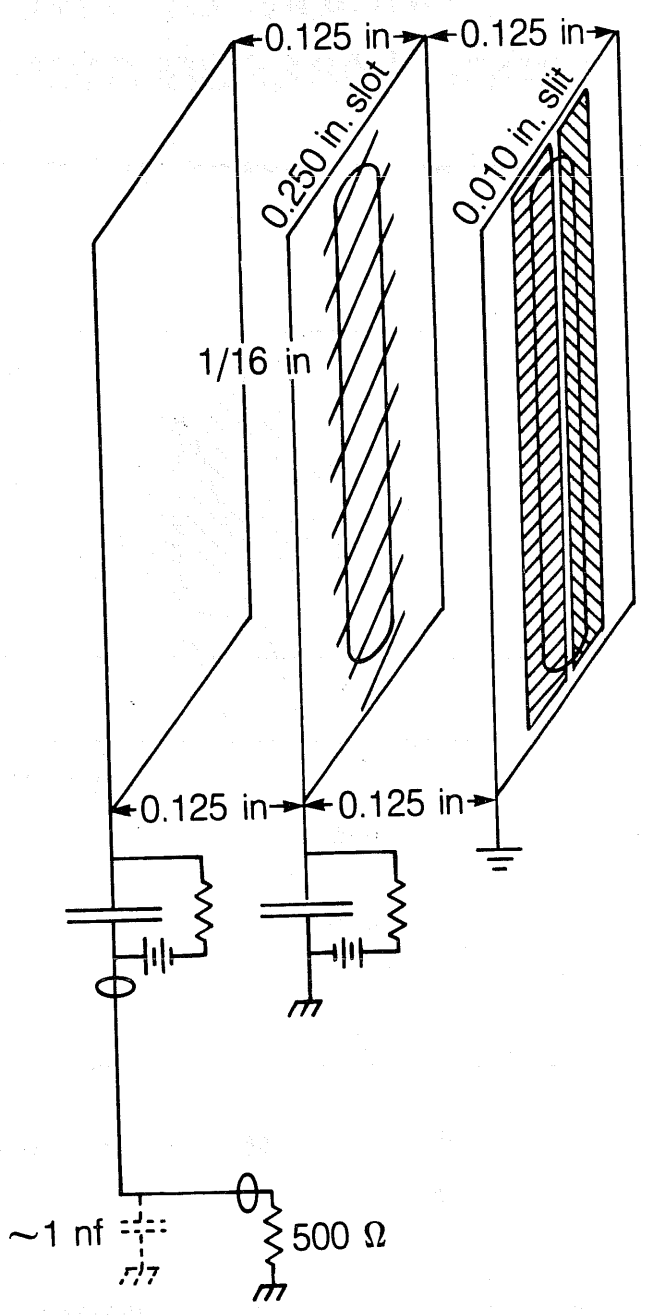

Figure 3.12: Diagram of the detectors we used for the slit measurements. The wires across the intermediate electrode provided a well-defined electrical surface over the slot.

3.5.5 Attenuator Wheel

We provided a wheel array (see Fig. 3.13) of attenuators and small apertures just downstream of the source and emittance grids. The attenuators were mesh screens 1.5 inches in diameter, ranging in transparency from 3.5% to 95%. The beam had a diameter of about 1 inch at the wheel location, and was well-centered within the apertures to avoid clipping part of the beam. We also provided several small apertures for current density scans across the source. We also used them for making small beamlets at various (x, y) positions over the source area to check source alignment and single-particle lattice properties. The small apertures were of 2 mm and 3 mm diameter; the 3 mm apertures were covered by a 50% transmission mesh. The motion across the source was nearly horizontal, because of the 4.75-inch radius from the center of the wheel to the center of the beam. Discrete vertical resolution was made possible by using apertures offset along radial lines from the wheel center, but was much poorer than the horizontal resolution.

3.6 Data Acquisition System

Data acquisition for phase space measurements and harp readout was done through a Tektronix 7D20 digitizing storage insert in a Tektronix 7904 oscilloscope, coupled to an HP-85 computer through the HPIB (IEEE-488) interface. The overall trigger and communication loop is shown in Fig. 3.14. The HP-85 controls the slits via a stepper motor interface, triggers the Marx generator and oscilloscope, and then interrogates the oscilloscope for the signal at a manually preset time. The HP-85 checks that the signal recorded by the oscilloscope is within the amplifier range setting, resets the amplifier gain, moves the slit(s) unless the signal was out-of-range, and continues the loop. The amplifier gain was set to keep the signal level near 1/3 of full-scale. This value was chosen because as the slits entered the beam, the beam signal

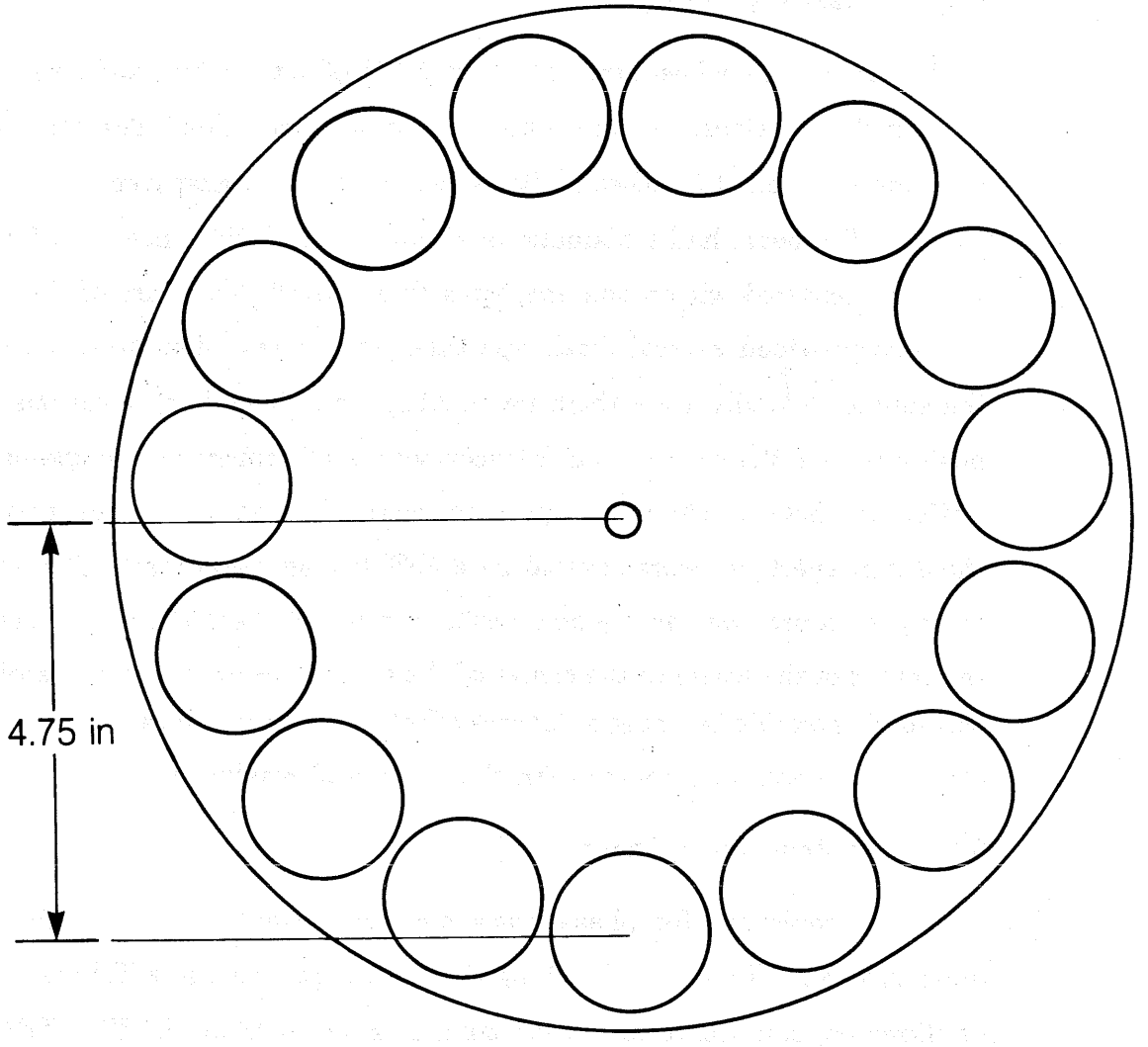

XBL 863-10352

Figure 3.13: Diagnostic wheel assembly. The holes in the wheel were of 1.5-inch diameter to avoid clipping the beam edges. Various attenuator grids were provided, along with blank inserts having either 2-mm or 3-mm diameter holes to generate beamlets for diagnostic purposes.

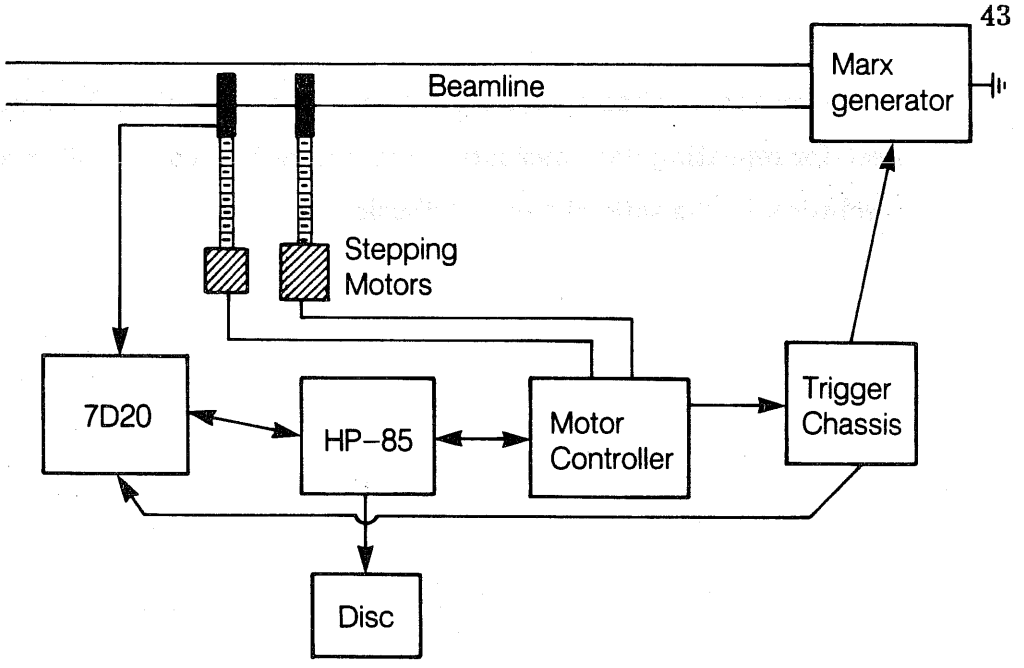

Automated data acquisition network physical layout

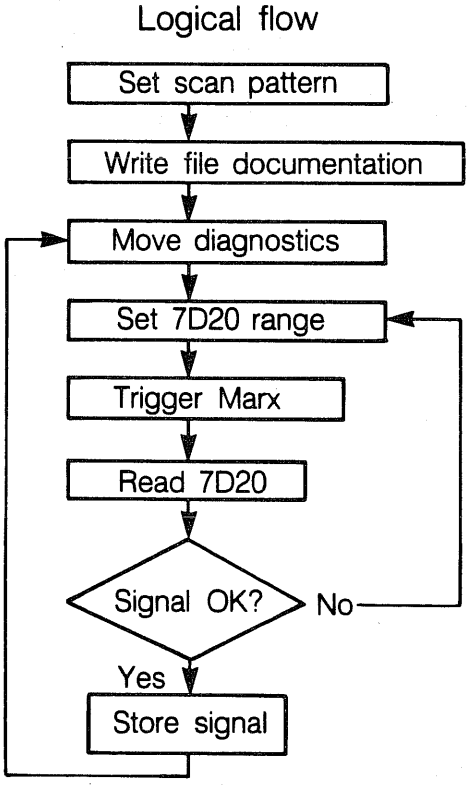

XBL 863-10350

Figure 3.14: HP-85 based data acquisition system layout and flow chart

rarely rose more than a factor of 3 from point to point. This minimized the need for repeating data measurements during the scans, while providing good resolution in the tails of the distribution.